

Large-eddy simulations of turbulent swirling flows injected into a dump chamber

By XIYUN LU†, SHANWU WANG, HONG-GYE SUNG‡, SHIH-YANG HSIEH¶ AND VIGOR YANG§

Department of Mechanical and Nuclear Engineering, The Pennsylvania State University, University Park, PA 16802, USA

(Received 12 October 2003 and in revised form 22 September 2004)

Turbulent swirling flows injected into a coaxial dump chamber at different swirl numbers were studied using large-eddy simulations. The Favre-filtered conservation equations of mass, momentum, and energy in three dimensions were solved numerically by means of a finite-volume approach. Results have been validated against experimental data in terms of mean flow velocity and turbulence properties. The work provides insight into several salient features of swirling flows, including vortex breakdown, shear-layer instability, and vortico-acoustic interactions. The dominant acoustic mode in the chamber was found to be sensitive to unsteady vorticity evolution, which in turn strongly depends on the swirl number. Low-frequency acoustic oscillations may arise from large-scale coherent motions in the central toroidal recirculation zone at high swirl numbers. In contrast, the shear-layer instability downstream of the backward-facing step results in high-frequency acoustic waves at low swirl numbers.

1. Introduction

Swirling flows are common in nature, as in tornadoes and whirlpools, and are utilized in a wide range of engineering applications. For example, they are used as an effective means of stabilizing flames and enhancing fuel/air mixing in combustion devices for propulsion and power-generation systems. Of practical interest in swirling flows is vortex breakdown, a phenomenon that manifests itself as an abrupt change in the core of a slender vortex, and usually develops downstream into a recirculating bubble or a spiral pattern. Because of the widespread occurrence of vortex breakdown, considerable effort has been devoted to achieving a better understanding of this phenomenon since its discovery by Peckham & Atkinson (1957) in their investigation of the flows over ‘Gothic’ wings. Comprehensive reviews on this subject have been written by Sarpkaya (1971*a, b*), Faler & Leibovich (1977*a, b*), Leibovich (1978, 1984), Shtern & Hussain (1999), and Lucca-Negro & O’Doherty (2001).

Sarpkaya (1971*a*) classified three types of breakdown in laminar swirling pipe flows: bubble, spiral, and double helix. The bubble mode usually predominates at high swirl numbers, while the spiral mode occurs at low swirl numbers. The double helix mode is formed when the vortex core expands and spirals, and is observed only in a diverging tube (Sarpkaya 1971*b*). These types of vortex breakdown are among the seven distinct modes of vortex core disruption revealed by Leibovich (1978) using

† Present Address: University of Science and Technology of China, Hefei, Anhui 230027, China.

‡ Present Address: Agency for Defense Development, Taejeon 305-600, South Korea.

¶ Present Address: General Electric Aircraft Engines, Cincinnati, OH 45215, USA.

§ Author to whom correspondence should be addressed: vigor@psu.edu

water flow visualization over a wide range of Reynolds and swirl numbers. At higher Reynolds numbers, the only characteristic geometric forms are the bubble and spiral modes (Leibovich 1984). Many investigations of vortex breakdown have focused on laminar flows with low Reynolds numbers (Grabowski & Berger 1976; Spall & Gatski 1991; Spall 1996). In practical applications such as swirl combustors, however, vortex breakdown occurs within turbulent flows. Although studies on laminar flows provide useful technical references, extension of these results to the turbulent regime is of questionable value. Sarpkaya (1995) and Sarpkaya & Novak (1998) presented experimental results on vortex breakdown in non-cavitating high-Reynolds-number turbulent swirling flows, and concluded that the resulting 'conical' breakdown is fundamentally distinct from the various forms of laminar vortex breakdown. The conical form of breakdown actually results from rapid precessing, in which the vortex core deviates slightly from the tube centreline. In spite of extensive studies conducted in the past few decades, a universally accepted explanation for the occurrence of vortex breakdown remains to be established (Shtern & Hussain 1999; Lucca-Negro & O'Doherty 2001). The presence of turbulence at high Reynolds numbers further complicates the problem. Understanding and characterizing turbulent swirling flows is still one of the fundamental challenges in fluid mechanics.

A large number of numerical studies have been performed on swirling flows. Lucca-Negro & O'Doherty (2001) conducted a systematic review of numerical simulations based on the Reynolds-averaged Navier–Stokes (RANS) equations. The RANS simulation may be appropriate for time-mean turbulent flow properties, but it may not describe unsteady flow evolution with high fidelity. Recent advances in large-eddy simulations (LES) have provided a powerful tool for studying the dynamics of turbulent swirling flows. Pierce & Moin (1998) examined a confined coaxial jet with swirl and heat release. A low-Mach-number variable-density formulation was implemented to account for the effects of heat release, along with an assumed PDF approach for modeling the subgrid-scale mixture fraction in the limit of infinitely fast chemistry. Kim, Menon & Mongia (1999) investigated turbulent fuel/air mixing in a gas turbine combustor using a conventional LES technique. Grinstein *et al.* (2002) explored unsteady non-reacting swirling flows in single- and triple-swirler nozzles by means of a monotone integrated large-eddy simulation (MILES) technique. Huang *et al.* (2003) and Huang & Yang (2004) studied the turbulent flame dynamics of a lean-premixed swirl-stabilized combustor based on a level-set flame library approach. The mutual couplings between acoustic motions, vortex shedding, and flame oscillations were examined. Those studies showed that the LES technique is capable of capturing salient flow structures and flame dynamics in turbulent environments. Only limited information about detailed flow evolution and the mechanisms driving acoustic motion in swirling flows appears in existing literature, however.

In this paper, a large-eddy simulation technique is utilized to study the turbulent swirling flows injected into a dump chamber, simulating the experiment conducted by Favaloro *et al.* (1989), as shown in figure 1. The purpose is to achieve an improved understanding of some of the fundamental phenomena in turbulent swirling flows, including turbulence properties, vortex breakdown, and unsteady flow development. Special attention is given to the effects of swirl on the generation of acoustic waves and their subsequent interactions with the shear-layer instability. In addition, a linear acoustic analysis is conducted to help identify the mechanisms of driving acoustic motions in the chamber. The paper is organized as follows. Sections 2 and 3 present the theoretical formulation and numerical method, respectively. The results are then described in §4, and the conclusions in §5.

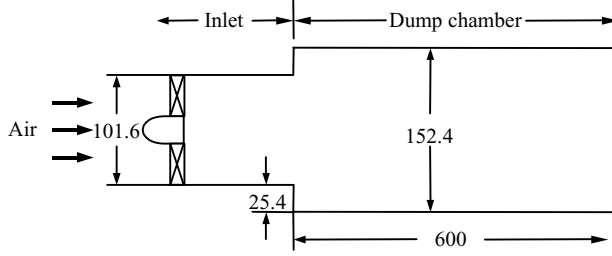


FIGURE 1. Schematic of a dump chamber with an inlet duct. Dimensions in mm.

2. Theoretical formulation

2.1. Filtered governing equations

Large-eddy simulations are implemented in the present work for turbulence closure, in which large-scale motions are explicitly computed and eddies with scales smaller than the grid or filter size are modelled to represent the effects of unresolved motions on resolved scales. The formulation is based on the Favre-filtered conservation equations of mass, momentum, and energy in three dimensions. The equations can be expressed in the following conservative form:

$$\frac{\partial \bar{\rho}}{\partial t} + \frac{\partial \bar{\rho} \tilde{u}_i}{\partial x_i} = 0, \quad (1)$$

$$\frac{\partial \bar{\rho} \tilde{u}_i}{\partial t} + \frac{\partial (\bar{\rho} \tilde{u}_i \tilde{u}_j)}{\partial x_j} = -\frac{\partial \bar{p}}{\partial x_i} + \frac{\partial (\tilde{\tau}_{ij} - \tau_{ij}^{SGS} + D_{ij}^{SGS})}{\partial x_j}, \quad (2)$$

$$\frac{\partial \bar{\rho} \tilde{E}}{\partial t} + \frac{\partial [(\bar{\rho} \tilde{E} + \bar{p}) \tilde{u}_i]}{\partial x_i} = \frac{\partial}{\partial x_i} (-\tilde{q}_i + \tilde{u}_j \tilde{\tau}_{ij} - Q_i^{SGS} + \sigma_i^{SGS} - H_i^{SGS}), \quad (3)$$

where an overbar denotes the spatial filter and a tilde the Favre filter, i.e. $\tilde{f} = \overline{\rho f} / \bar{\rho}$. The variables ρ , u_i , p , and E represent the density, velocity component, pressure, and specific total energy, respectively. The diffusive fluxes are given by

$$\tilde{\tau}_{ij} = 2\tilde{\mu} \tilde{S}_{ij} - \frac{2}{3}\tilde{\mu} \delta_{ij} \tilde{S}_{kk}, \quad (4)$$

$$\tilde{q}_i = -\tilde{k} \frac{\partial \tilde{T}}{\partial x_i}. \quad (5)$$

Here, μ and k are the molecular viscosity and thermal conductivity, respectively. The strain-rate tensor S_{ij} is defined as $S_{ij} = (\partial u_j / \partial x_i + \partial u_i / \partial x_j) / 2$. The equation of state for an ideal gas is used.

The subgrid closure terms are defined as

$$\tau_{ij}^{SGS} = \bar{\rho} (\tilde{u}_i \tilde{u}_j - \bar{u}_i \bar{u}_j), \quad (6)$$

$$D_{ij}^{SGS} = (\tilde{\tau}_{ij} - \tau_{ij}^{SGS}), \quad (7)$$

$$Q_i^{SGS} = (\bar{q}_i - \tilde{q}_i), \quad (8)$$

$$H_i^{SGS} = \bar{\rho} (\tilde{E} \tilde{u}_i - \tilde{E} \bar{u}_i) + (\bar{p} \bar{u}_i - \bar{p} \tilde{u}_i), \quad (9)$$

$$\sigma_i^{SGS} = (\bar{u}_j \tau_{ij} - \tilde{u}_j \tilde{\tau}_{ij}). \quad (10)$$

These terms arise from unresolved scales and need to be modelled in terms of resolved scales. Because the filter scale of LES falls in the inertial subrange of the turbulent

kinetic energy spectrum, the modelling of subgrid terms is relatively universal in comparison with that of the RANS simulation.

2.2. Subgrid-scale models

The introduction of the dynamic model (Germano *et al.* 1991) has spurred significant progress in the subgrid-scale (SGS) modeling of non-equilibrium flows. Among the various SGS turbulence models, such as the mixed model (Fureby 1996) and the two-parameter mixed model (Salvetti & Banerjee 1995), the dynamic SGS model for turbulence closure offers the best tradeoff between accuracy and cost (DesJardin & Frankel 1998). In the present study, the Smagorinsky dynamic model for compressible flows proposed by Moin *et al.* (1991) is employed. The anisotropic part of the SGS stresses, (6), is treated using the Smagorinsky model (Smagorinsky 1963), while the isotropic part, τ_{kk}^{SGS} , is modeled with a formulation proposed by Yoshizawa (1986),

$$\tau_{ij}^{SGS} - \frac{1}{3}\delta_{ij}\tau_{kk}^{SGS} = -2C_R\bar{\Delta}^2\bar{\rho}|\tilde{\mathbf{S}}|(\tilde{S}_{ij} - \frac{1}{3}\delta_{ij}\tilde{S}_{kk}) = C_R\alpha_{ij}, \quad (11)$$

$$\tau_{kk}^{SGS} = 2C_I\bar{\rho}\bar{\Delta}^2|\tilde{\mathbf{S}}|^2 = C_I\alpha, \quad (12)$$

where $\alpha_{ij} = -2\bar{\Delta}^2\bar{\rho}|\tilde{\mathbf{S}}|(\tilde{S}_{ij} - \delta_{ij}\tilde{S}_{kk}/3)$, $\alpha = 2\bar{\rho}\bar{\Delta}^2|\tilde{\mathbf{S}}|^2$. C_R and C_I are model constants and are determined dynamically during calculation. The model utilizes the information about resolved scales at the grid-filter level and at a coarser test-filter level with $\hat{\Delta} > \bar{\Delta}$. The least-squares method proposed by Lilly (1992) is then implemented to obtain the two model parameters,

$$C_R = \frac{\langle L_{ij}M_{ij} \rangle}{\langle M_{kl}M_{kl} \rangle} - \frac{1}{3} \frac{\langle L_{mm}M_{nn} \rangle}{\langle M_{kl}M_{kl} \rangle}, \quad (13)$$

$$C_I = \frac{\langle L_{kk} \rangle}{\langle \beta - \hat{\alpha} \rangle}. \quad (14)$$

The brackets $\langle \cdot \rangle$ denotes local smoothing in the test filter (Fureby 1996; DesJardin & Frankel 1998), which is used to circumvent the numerical instability originating from the dynamic calculation of the coefficients of the eddy-viscosity model (Moin *et al.* 1991; Germano *et al.* 1991). A local volume-weighted average with around 27 points is employed. Additional clipping based on the entropy-limit condition of the form $\mu + \mu_T \geq 0$ is implemented to limit the extent of backscattering in the calculation, where μ_T is the SGS turbulent viscosity. In the present study, the fraction of grid points requiring additional clipping is less than 1%. The explicit forms of L_{ij} , M_{ij} and β are

$$L_{ij} = \widehat{\rho\tilde{u}_i\tilde{u}_j} - \hat{\rho}\tilde{u}_i\tilde{u}_j = \widehat{\rho u_i \rho u_j} / \hat{\rho} - \widehat{\rho u_i} \widehat{\rho u_j} / \hat{\rho}, \quad (15)$$

$$M_{ij} = \beta_{ij} - \hat{\alpha}_{ij}; \quad \beta_{ij} = -2\hat{\Delta}^2\hat{\rho}|\tilde{\mathbf{S}}|(\tilde{S}_{ij} - \delta_{ij}\tilde{S}_{kk}/3); \quad \beta = 2\hat{\rho}\hat{\Delta}^2|\tilde{\mathbf{S}}|^2, \quad (16)$$

where the hat represents the test-filtered variable. A Favre-filtered variable at the test-filter level is defined as $\tilde{f} = \widehat{\rho f} / \hat{\rho}$.

The subgrid energy flux term, H_i^{SGS} , is modelled as

$$H_i^{SGS} = -\bar{\rho} \frac{v_t}{Pr_t} \frac{\partial \tilde{H}}{\partial x_i} = -\bar{\rho} \frac{v_t}{Pr_t} \left(\frac{\partial \tilde{h}}{\partial x_i} + \tilde{u}_j \frac{\partial \tilde{u}_j}{\partial x_i} + \frac{1}{2} \frac{\partial k^{SGS}}{\partial x_i} \right) \quad (17)$$

where \tilde{H} represents the filtered specific total enthalpy. The turbulent Prandtl number, Pr_t , takes a conventional value of 0.7 (Zang, Dahlburg & Dahlburg 1992). The SGS kinetic energy term, k^{SGS} ,

$$k^{SGS} = \frac{1}{2}(\widehat{u_i u_i} - \tilde{u}_i \tilde{u}_i) \quad (18)$$

is formulated using the model proposed by Yoshizawa (1986). The SGS viscous diffusion term, σ_i^{SGS} , is neglected in the present study due to its small contribution in the energy equation (Martin *et al.* 2000). The nonlinearity of the viscous stress term, D_{ij}^{SGS} , and the heat flux term, Q_i^{SGS} , is invariably neglected (Piomelli 1999).

2.3. Boundary conditions

The flow under consideration is subsonic and confined in a volume reaching from the downstream end of the swirl vanes to the chamber exit, as shown in figure 1. The no-slip, adiabatic conditions are applied to all the solid walls. The boundary conditions at the outlet and inlet are specified according to the method of characteristics.

At the outlet, extrapolation of primitive variables from the interior region may cause undesirable reflection of waves propagating into the computational domain. The non-reflecting boundary conditions based on the characteristic equations proposed by Poinso & Lele (1992) are applied. A reference pressure, p_r , is utilized to preserve the average pressure in the computational domain through small-amplitude acoustic waves originating from a virtual boundary. If the chamber exit pressure differs from the reference quantity, information will propagate to the boundary to adjust the pressure to a prespecified value. The reference pressure can be obtained using a simplified radial momentum equation

$$\frac{\partial p_r}{\partial r} = \frac{\rho U_\theta^2}{r} \quad (19)$$

at the exit, where U_θ is the long-time-averaged azimuthal velocity. Because the azimuthal velocity at the exit is small, a uniform distribution of the reference pressure eventually leads to the same result as that from (19). Thus, a constant reference pressure is employed in the present study for convenience. It should be noted that the present treatment of boundary conditions is not perfectly non-reflecting due to the introduction of the reference pressure. Low-frequency acoustic waves may be partially reflected into the flow field (Polifke & Wall 2002). The corresponding cutoff frequency depends on the chamber geometry and flow condition, as well as the relaxation coefficient, σ , in the characteristic equation determining the temporal variation of the incoming acoustic-wave amplitude. An appropriate value of σ should be selected to keep the cutoff frequency much lower than the frequency range of concern.

To specify the instantaneous inlet flow conditions, the flow properties are decomposed into the mean, acoustic, and turbulent components, e.g. $p = \bar{p} + p'_a + p'_t$ (Huang *et al.* 2003). The acoustic part can be written as a synthesis of the Fourier components

$$p'_a(t) = \text{Re} \left[\sum_1^L \hat{p}_{a,n}(\omega_n) e^{i\omega_n t} \right], \quad (20)$$

where ω denotes frequency. For the mean flow properties, the total temperature and velocity are specified, and the pressure is determined based on a one-dimensional approximation to the momentum equation in the direction normal to the inlet boundary. Owing to the lack of experimental information at the inlet, the flow velocity profile at the inlet is tuned to match the experimental data at the first measurement position, $x/H = 0.38$. The axial velocity profile bears a close resemblance to that described by the 1/7-power law. The radial velocity is nearly zero, and the azimuthal component is determined by the swirler vane angle.

Because the vortico-acoustic interaction is one of the major foci of the current study, the inlet acoustic boundary must be treated carefully. Due to the presence of the swirler vanes, which are difficult to simulate numerically, the non-reflecting boundary

condition of Poinso & Lele (1992) cannot be simply implemented at the inlet. It is well established that the acoustic waves generated in the dump chamber propagate both upstream and downstream. On reaching the swirler vanes, the upstream-running wave will be partially reflected back and partially transmitted upstream through the vanes. The acoustic reflection and transmission properties can only be expressed in terms of the acoustic admittance function, A_d , defined as

$$\hat{A}_d(\omega_n) = \frac{\hat{u}_{a,n}(\omega_n)/\bar{c}}{\hat{p}_{a,n}(\omega_n)/\gamma\bar{p}}. \quad (21)$$

Here γ and \bar{c} denote the ratio of specific heats and the mean speed of sound, respectively. The admittance function can be obtained either from impedance-tube experiments for the swirler, or by matching the measured acoustic field for a given physical configuration (Broda *et al.* 1998). The corresponding acoustic velocity takes the form

$$u'_a(t) = (\bar{c}/\gamma\bar{p}) \operatorname{Re} \left[\sum_1^L \hat{A}_d(\omega_n) \hat{p}_{a,n}(\omega_n) e^{i\omega_n t} \right] \quad (22)$$

In the present study, a zero acoustic admittance is utilized to represent an acoustically closed boundary. This condition simulates a physical configuration in which perforated plates (i.e. a flow straightener) are placed in front of the swirler vanes.

Turbulence is provided by superimposing broadband noise with a Gaussian distribution on the mean velocity profile. The effect of the inlet turbulence on the flow development seems to be modest. The turbulence intensity was varied by 50% from its nominal value of 10% of the mean flow quantity at the inlet, but very little impact was observed on the result. This may be attributed to the strong shear layers and high-intensity turbulence generated in the flow field, which overshadow the influence of the incoming turbulence.

3. Numerical method

The theoretical formulation is numerically solved by means of a density-based finite-volume approach, which allows the treatment of arbitrary geometry and avoids the problems with metric singularities usually associated with finite-difference methods. Spatial discretization is achieved using a fourth-order central differencing scheme developed by Rai & Chakravarthy (1993). A sixth-order scalar artificial dissipation term is employed to prevent numerical oscillations. Temporal integration is performed using an explicit four-step Runge–Kutta scheme (Jameson 1983).

Apte & Yang (2001) conducted a comprehensive analysis of numerical errors associated with several common algorithms within the context of LES, extending the approach of Fabignon, Beddini & Lee (1997). The errors arising from the convection, artificial viscosity, and SGS terms were assessed by introducing a reference turbulent kinetic energy spectrum obtained from isotropic turbulence theory. Following the same methodology and substituting the artificial viscosity term used in the present study, $\varepsilon_6 = 0.001$, it was found that the numerical dissipation is smaller than the SGS term as shown in figure 2. This figure shows the normalized spectrum of the turbulent kinetic energy, $E(k, \tau)$, after one eddy turnover time, τ , for isotropic turbulence with Mach number, $M = 0.6$, Reynolds number, $Re = 4.51 \times 10^5$, CFL number, $CFL = 0.6$, and grid parameter, $\xi = \Delta x/\eta = 50$. Here k , Δx and η , denote the wavenumber, grid size, and Kolmogorov scale, respectively. Figure 2 indicates that the present numerical method offers a reasonable predictive capability for turbulent flows because of its relatively low dissipation and high accuracy.

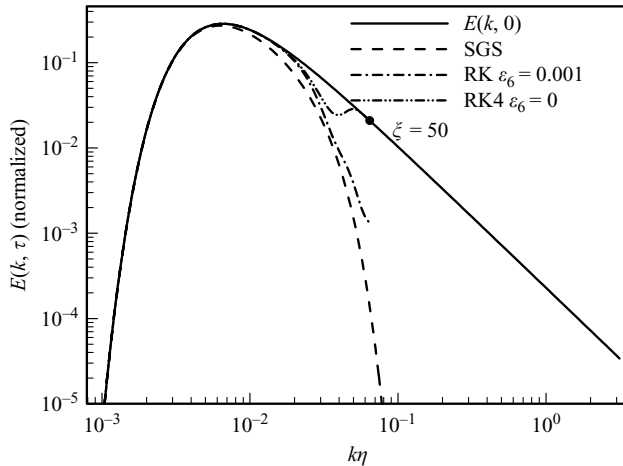


FIGURE 2. Comparison of effects of artificial dissipation and SGS terms on the turbulent kinetic energy spectrum based on the four-step Runge–Kutta scheme along with fourth-order central differencing (RK4-4C) scheme. $Re = 4.51 \times 10^5$, $M = 0.6$, $\xi = 50$, $CFL = 0.6$.

The code is further equipped with a multi-block domain decomposition feature to facilitate parallel processing in a distributed computing environment using the Message Passing Interface (MPI) library. The parallelization methodology is robust and the speedup is almost linear. A detailed description of the numerical architecture is given by Wang (2002).

4. Results and discussion

The detailed flow structures and acoustic-wave evolution in the swirl chamber shown in figure 1 were studied in depth. The work simulates the experiment conducted by Favaloro *et al.* (1989). A swirler with 12 circular inlet guide vanes is located 50.8 mm upstream of the dump plane. The leading edge of each blade is designed to be tangential to the incoming flow and perpendicular to the centreline of the chamber. The chamber consists of a Plexiglas pipe measuring 152.4 mm in diameter and 1850 mm in length. The inlet temperature and pressure are 300 K and 1 atm, respectively. The Reynolds number is 1.25×10^5 based on the inlet diameter. The centreline velocity in the inlet pipe, $U = 19.2 \text{ m s}^{-1}$, and the height of the backward-facing step, $H = 25.4 \text{ mm}$, are used as the reference quantities to normalize the flow properties. The detailed configuration of the experimental rig, which can be found in Favaloro *et al.* (1989), is omitted for the sake of clarity. Two swirl numbers ($S = 0.3$ and 0.5), defined as the ratio of the axial flux of the angular momentum to that of the axial momentum divided by the inlet radius, are considered. More emphasis is placed on the $S = 0.5$ case because of the occurrence of vortex breakdown. The situation with $S = 0.3$, in which vortex breakdown is not observed, is treated for comparison.

The computational domain consists of the inlet duct immediately downstream of the swirler and includes the entire dump chamber. A three-dimensional grid is generated by rotating a two-dimensional grid with respect to the centreline. The total grid numbers are $161 \times 75 \times 81$ in the axial, radial, and azimuthal directions, respectively. The grid is uniform in the azimuthal direction, but stretched in the axial and radial directions in order to resolve rapid flow variations in the shear-layer and near-wall regions. The mean cell size in the upstream region of the chamber is around

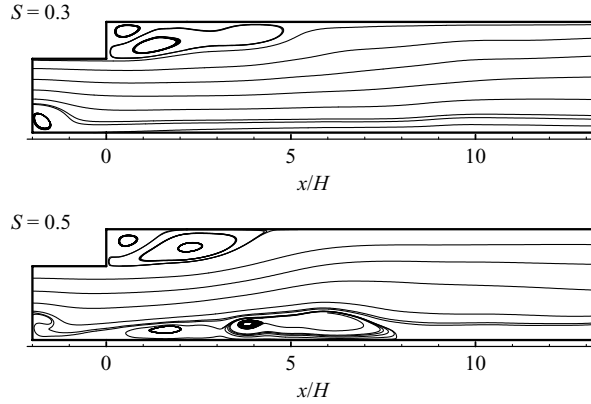


FIGURE 3. Streamlines based on mean axial and radial velocity components; swirl numbers $S=0.3$ and 0.5 .

2 mm, which falls roughly in the inertial subrange of the turbulent kinetic energy spectrum based on the Reynolds number. The spatial resolution near the wall spans from $y^+ = 2$ to 6, which is within the viscous sub-layer. The computational domain is divided into 28 subdomains for parallel processing.

The CFL number is 0.9 and the physical time step is around 5×10^{-5} ms. For each swirl number, the calculation is performed over an extended time period to ensure the establishment of a stationary flow field. Data are then collected for about 3 flow-through times (i.e. 66 ms) to obtain statistically meaningful turbulence properties.

4.1. Flow evolution and vortex breakdown

The streamlines of the time-mean flow field based on the axial and radial velocities are presented in figure 3. Both the primary and secondary separation bubbles are observed in the downstream region of the backward-facing step. The length of the corner recirculation zone (CRZ) is shorter for the high swirl-number case ($S=0.5$) due to the stronger expansion of the main flow resulting from the higher centrifugal force. A small separation bubble exists behind the centrebody and the flow rapidly merges along the centreline. The result is consistent with the experimental observation by Favalaro *et al.* (1989).

A simplified momentum equation indicates that a radial pressure gradient is produced by the centrifugal force arising from the swirling effect:

$$\frac{\partial p}{\partial r} = \frac{\rho U_\theta^2}{r}. \quad (23)$$

The pressure tends to be minimized in regions where strong swirling motions occur, i.e. in the wake of the centrebody. As the flow expands and the azimuthal velocity decays with the axial distance, the pressure is recovered in the downstream region. Consequently, a positive pressure gradient is generated along the axial axis, which may lead to the formation of a recirculating flow in high-swirl flows, a phenomenon commonly termed ‘vortex breakdown’.

Vortex breakdown occurs only at high swirl numbers, as shown in figure 3. A toroidal recirculation zone (CTRZ) is formed in the central region for $S=0.5$, reaching from $x/H \approx 0.36$ to 7.8. This kind of vortex breakdown is different from the patterns observed in previous experiments, and cannot be classified as of the bubble, spiral, or conical type. Figure 4 shows the mean azimuthal velocity field, one of the key factors

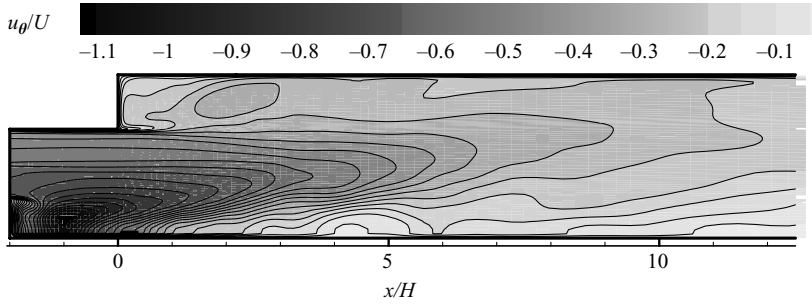


FIGURE 4. Contours of mean azimuthal velocity, swirl number $S = 0.5$.

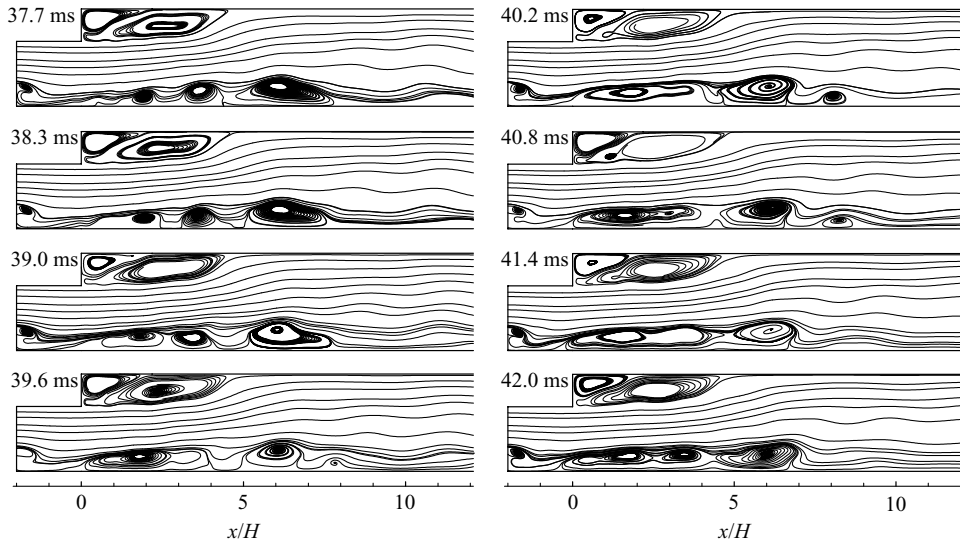


FIGURE 5. Time evolution of streamlines based on mean axial and radial velocity components spatially averaged in the azimuthal direction (time increment of 0.6 ms), swirl number $S = 0.5$.

dictating the occurrence of vortex breakdown, for $S = 0.5$. Because the centrebody is quite small, the flow merges quickly toward the centreline after passing over it. The conservation of angular momentum gives rise to a high azimuthal velocity during this merging process. The maximum azimuthal velocity occurs in the region between $x/H \approx -1.21$ and -0.43 , where the pressure reaches its local minimum. The azimuthal velocity decays in the downstream region because of flow expansion and viscous dissipation. An adverse pressure gradient develops along the axial direction, which subsequently results in the presence of a central recirculating flow starting from $x/H \approx 0.36$.

The temporal evolution of the flow field is examined to explore the phenomenon of vortex breakdown. Figure 5 shows the instantaneous streamlines on an (x, r) -plane, spatially averaged in the azimuthal direction, at various times during a typical flow evolution period. The time increment between the snapshots is 0.6 ms, and $t = 0$ corresponds to the instant at which data collection begins after the flow reaches its stationary state. At $t = 37.7$ ms, a new vortical bubble is generated in front of a braid of vortical bubbles. These bubbles then coalesce at $t = 39.0$ ms. The bubble located in the downstream side of the vortical braid is separated into two structures

at $t = 39.6$ ms; one stays at basically the same location, and the other is convected downstream and finally disappears due to turbulent diffusion and viscous dissipation at $t = 41.4$ ms. During this period, the coalesced vortical bubble separates, and another new bubble appears in the upstream region at $t = 42.0$ ms. These snapshots exhibit a very complicated vortex evolution in the central region.

4.2. Mean flow-field and turbulence characteristics

To validate the present analysis and to characterize turbulent swirling flows, this section compares numerical and experimental data (Favaloro *et al.* 1989) in terms of mean velocity, turbulence intensities, and turbulent kinetic energy.

4.2.1. Mean velocity profiles

Figure 6 shows the radial distributions of the time-mean axial, radial, and azimuthal velocity components at the three measurement locations $x/H = 0.38, 1.0$ and 4.0 . The swirl number is 0.5. Reasonable agreement is obtained with the experimental measurements of Favaloro *et al.* (1989).

The negative axial velocity near the centreline indicates the existence of a central recirculation zone. Flow reversal is also observed in the corner region ($r/H > 2$). The axial velocity profile at $x/H = 0.38$ is similar to that at the inlet and smoothly develops to a parabolic shape in the downstream region ($x/H = 4.0$) due to flow expansion and turbulent diffusion. The weak radial momentum in the inlet and the geometrical confinement render the radial velocity considerably smaller than the other two components. The flow gradually spreads in the radial direction because of the centrifugal effect, leading to a positive radial velocity in the main flow passage. The rapid variation in the corner region results from the sudden expansion of the geometry and the existence of a recirculating flow.

Two points should be noted here concerning the azimuthal velocity plots shown in figure 6. First, the linear profile of the azimuthal velocity in the central toroidal recirculation zone bears a strong resemblance to that of a solid-body rotation, and is insensitive to the occurrence of flow reversal. Similar behaviours were previously observed in many experimental and numerical studies on swirling flows, such as Panda & McLaughlin (1994), Billant, Chomaz & Huerre (1998), Pierce & Moin (1998), Paschereit, Gutmark & Weisenstein (1999), and Wang (2002). One factor contributing to this phenomenon is the strong vorticity in the slender core region, whose time-averaged distribution to first approximation can be treated as uniform because of the high-intensity tangential motion and turbulent mixing in the core region. Therefore, a first-order Taylor expansion of the azimuthal velocity profile, i.e. linear distribution, represents a good approximation in the vortex core region. Another factor is that as in the Rankine vortex core the internal attenuation of flow motion with a linearly distributed azimuthal velocity is relatively weak, so that vorticity strength is preserved. The second point is that the present analysis underpredicts the azimuthal velocity near the wall. This deficiency may be attributed to the lack of reliable data specifying the inlet flow conditions, which may exert significant influence on the results (Grinstein *et al.* 2003).

All the velocity profiles indicate a decrease in the maximum velocity magnitude and an increase in the radial location at which the maximum velocity occurs in the downstream region. In addition to turbulent diffusion and viscous dissipation, the swirling effect and the rapid flow expansion arising from the chamber geometrical variation across the dump plane contribute substantially to the observed phenomena. As a consequence, the axial and azimuthal velocities decrease to satisfy the conservation

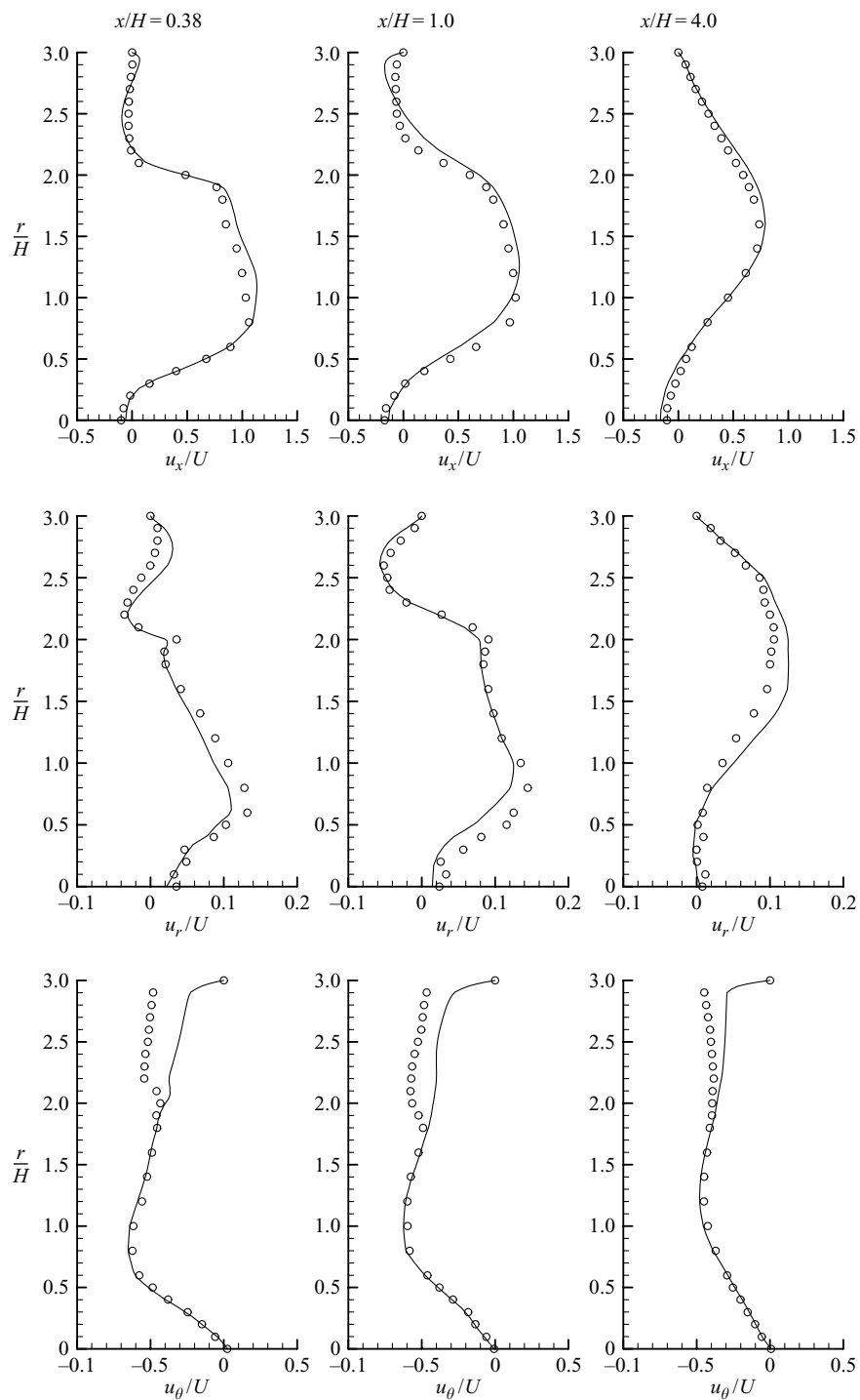


FIGURE 6. Radial distributions of mean velocity components at different axial locations (line: computation; symbol: experiment, Favalaro *et al.* 1989), swirl number $S = 0.5$.

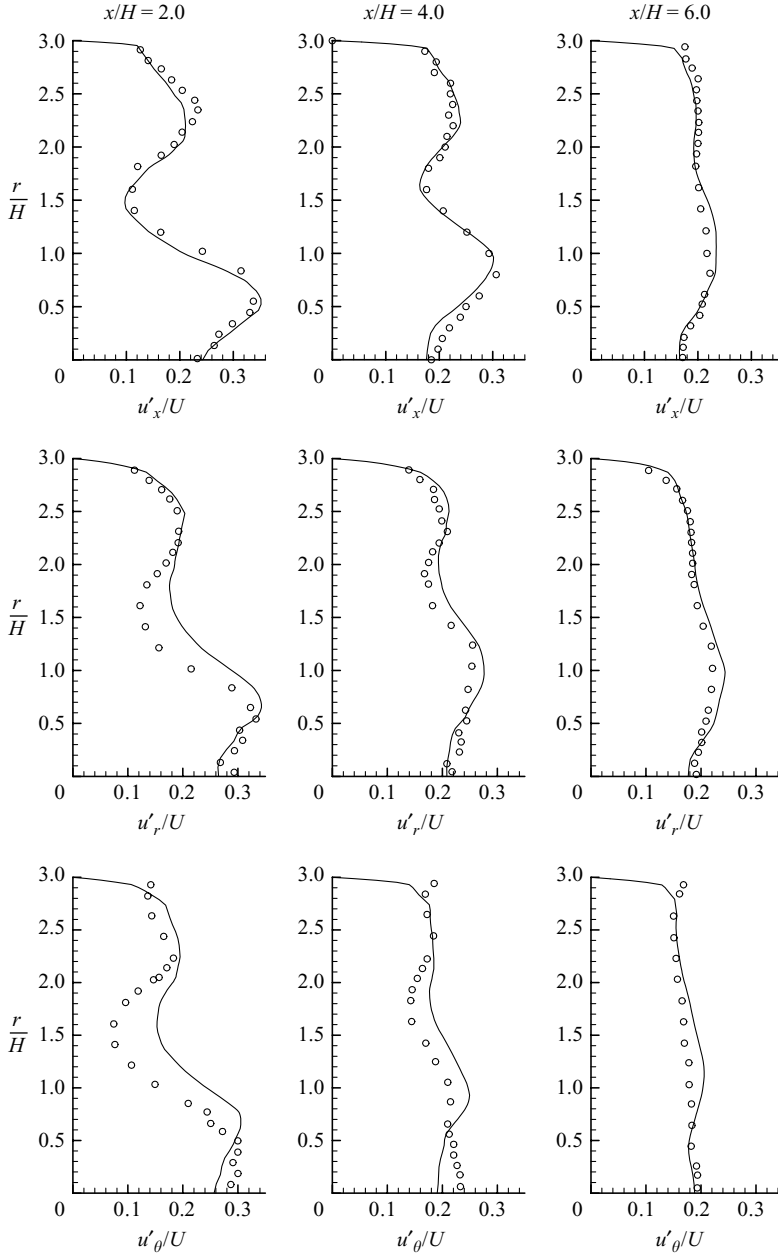


FIGURE 7. Radial distributions of turbulence intensities at different axial locations (line: computation; symbol: experiment, Favaloro *et al.* 1989), swirl number $S = 0.5$.

of mass and angular momentum. The entire process promotes the pressure recovery in the downstream region, and leads to the occurrence of vortex breakdown, especially for high-swirl-number flows.

4.2.2. Turbulence intensities and turbulent kinetic energy

Figure 7 shows the radial distributions of the normalized turbulence intensity components at three measurement locations, $x/H = 2.0$, 4.0 , and 6.0 . The distributions of

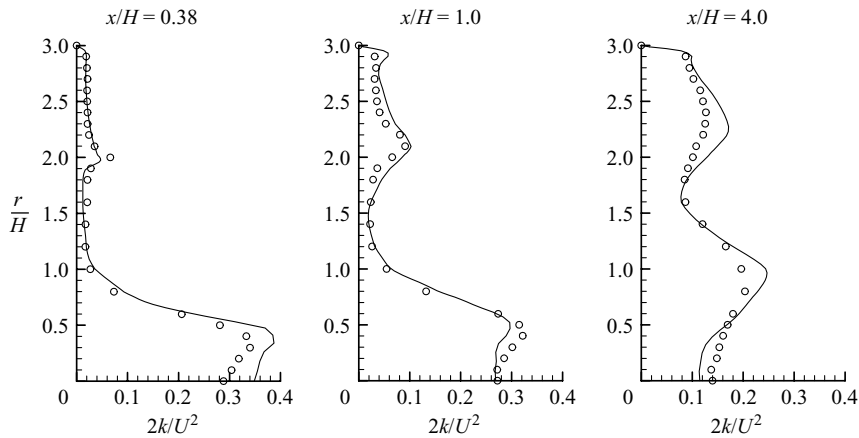


FIGURE 8. Radial distributions of turbulent kinetic energy at different axial locations (line: computation; symbol: experiment, Favalaro *et al.* 1989), swirl number $S = 0.5$.

the turbulent kinetic energy, k , are given in figure 8. Two peaks, resulting from the strong shear layers originating from the centrebody and the backward-facing step, are observed on the profiles of the turbulence intensities at $x/H = 2.0$. The development in the downstream region is similar to that of the mean velocity profiles, which expand radially and become more uniform as the flow evolves. The smooth distributions of the three turbulence intensity components and their approximately equal magnitudes in the downstream region suggest that turbulence tends to become isotropic as a result of the diffusion and dissipation effects. This redistribution process usually proceeds much faster than that in non-swirling flows because of the swirling effect. The high turbulence intensity in the central region (see figure 8) resulting from the unsteadiness of the vortex core produces rapid fluid mixing within the recirculation region.

4.3. Instantaneous flow field

The present flow field involves an array of intricate phenomena, including the Kelvin–Helmholtz instability, vortex breakdown, and centrifugal instability (Panda & McLaughlin 1994; Martin & Meiburg 1996). Figure 9 shows two instantaneous axial velocity fields for swirl numbers of 0.3 and 0.5. Shear layers are produced at the trailing edges of the centrebody and the backward-facing step due to the Kelvin–Helmholtz instabilities in both the axial and azimuthal directions. The flow evolution in the azimuthal direction is presented on the two cross-sections at $x/H = 0.36$ and 1.54. The shear layer originating from the backward-facing step remains almost symmetric immediately downstream of the dump plane ($x/H = 0.36$). It then rolls up and forms large asymmetric structures at $x/H = 1.54$, because of the strong shear force in the azimuthal direction.

The large velocity difference in the azimuthal direction at a high swirl number ($S = 0.5$) significantly increases the strength of the shear layer, especially around the boundary of the central toroidal recirculation zone. As a consequence of flow reversal, the effective flow passage area in the chamber is reduced, which hence increases the axial velocity difference and further enhances the shear layer in the axial direction. The large-scale structures are eventually dissipated by turbulent diffusion and viscous damping when the flow convects downstream.

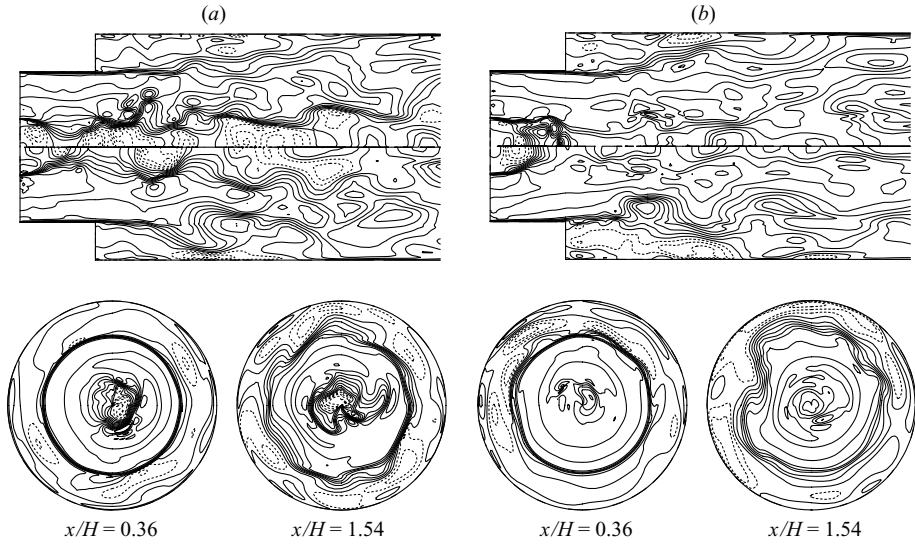


FIGURE 9. Instantaneous axial velocity fields on an (x, r) -plane and two cross-sections, $x/H = 0.36$ and 1.54 . Contour levels between -12 and 33 m s^{-1} with increment of 3 m s^{-1} . Solid lines: positive values; dashed lines: negative values. (a) Swirl number $S = 0.5$ and (b) swirl number $S = 0.3$.

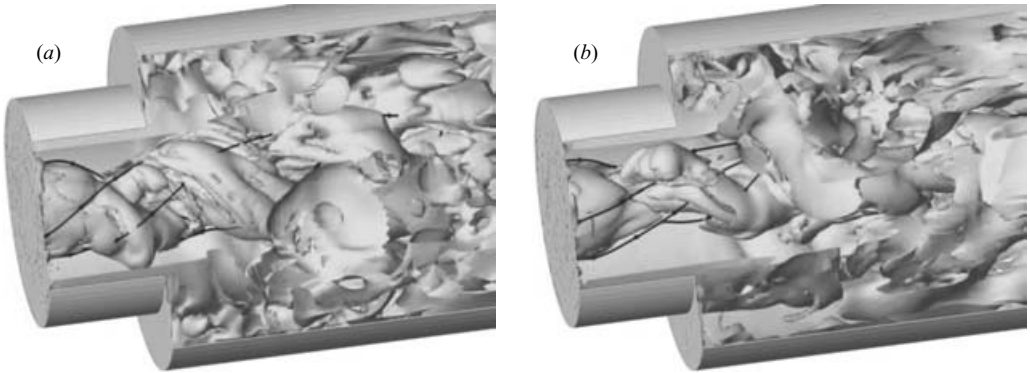


FIGURE 10. Snapshots of iso-surfaces of vorticity magnitude at $1.5 \times U/H$. Dark lines represent streamlines. (a) Swirl number $S = 0.5$ and (b) swirl number $S = 0.3$.

Figure 10 shows snapshots of the iso-surfaces of vorticity magnitude at $|\Omega| = 1.5U/H$ (i.e. 1133 s^{-1}) for $S = 0.3$ and 0.5 . Helical vortex tubes develop from the inlet and travel in a direction opposite to the main swirling flow, although the whole structure follows the motion of the main flow. The swirl number plays an important role in dictating the flow evolution and its underlying mechanisms. The helical structure at $S = 0.5$ arises from the vortex breakdown and expands in the downstream region. The situation is different, however, for a low swirl number, in which the helical structure of the vortex tube shrinks in the downstream region. This phenomenon may be attributed to the precession of the vortex core around the centreline. The resultant intermittent occurrence of vortex breakdown causes the helical structure issued from the centrebody to vanish rapidly as the flow evolves downstream. A high swirl number apparently helps maintain flow coherence and leads to strong flow reversal.

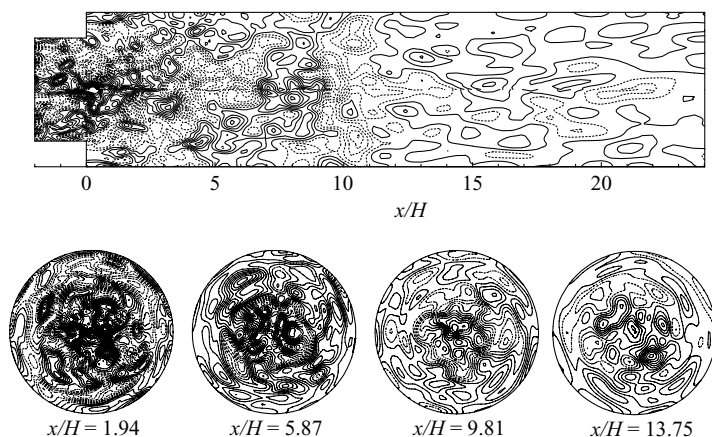


FIGURE 11. Instantaneous fluctuating pressure field on an (x, r) -plane and cross-sections at $x/H = 1.94, 5.87, 9.81,$ and 13.75 . Contour levels between -600 and 600 Pa with increment of 50 Pa. Solid lines: positive values; dashed lines: negative values. Swirl number $S = 0.5$.

4.4. Acoustic field

The strong vortical motion in the chamber often produces acoustic waves propagating throughout the entire field. The shear layers, on the other hand, are susceptible to acoustic excitations if such disturbances occur at appropriate locations and frequencies. A feedback loop can thus be established, depending on the mutual coupling between the vortical and acoustic fields. To explore vortico-acoustic interaction, the fluctuating pressure field is obtained by subtracting the long-time-averaged pressure from its instantaneous quantity.

Figure 11 shows snapshots of the fluctuating pressure field on several cross-sections for the high-swirl-number case with $S = 0.5$. Considerable pressure fluctuations take place immediately downstream of the centrebody, where strong vorticity is present. The entire field exhibits a wide range of length scales, with broadband turbulent motion in the upstream region which develops into large-scale coherent acoustic motion in the downstream region. To help identify the wave characteristics, especially those associated with longitudinal waves, the complicated three-dimensional field shown in figure 11 is spatially averaged in the azimuthal direction. Figure 12 presents the time sequence of the resultant quasi-two-dimensional fields. The data are further reduced by spatial averaging over each cross-section along the axial axis. The averaged quasi-one-dimensional fields shown in figure 13 indicate that a negative pressure peak, followed by a positive one, forms periodically and travels downstream at the speed of sound. Two negative pressure peaks are observed in the chamber at $t = 35.9$ ms. Because the evolution patterns of these two fluctuations are almost identical, we conclude that the frequency of the pressure wave is approximately 655 Hz, based on the distance between the two pressure peaks at $t = 35.9$ ms and the wave propagation speed.

As mentioned in §2.3, the downstream boundary conditions are not perfectly non-reflecting. Low-frequency acoustic waves may be partially reflected into the flow field due to the introduction of the reference pressure. The cutoff frequency, below which flow disturbances may propagate into the computational domain, can be estimated following the method described by Polifke & Wall (2002). In the present study, the relaxation coefficient σ in the characteristic equation is taken to be 0.25 and the chamber length is 0.6 m. The resultant cutoff frequency of 100 Hz is much smaller

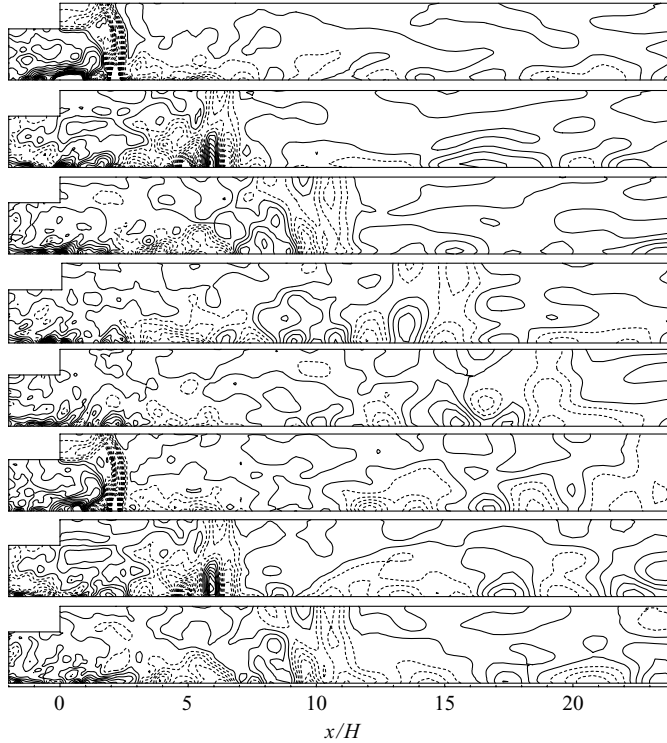


FIGURE 12. Time evolution of fluctuating pressure field spatially averaged in the azimuthal direction. Contour levels between -600 and 600 Pa with increment of 50 Pa (time increment of 0.3 ms). Solid lines: positive values; dashed lines: negative values. Swirl number $S = 0.5$.

than the oscillation frequencies of concern (i.e. greater than 600 Hz). The treatment of the downstream boundary conditions appears to be appropriate.

4.4.1. Vortico-acoustic interactions

The frequency spectra of pressure fluctuations are obtained to quantitatively characterize the acoustic flow evolution. Figure 14 shows the result at $y/H = 0.06$ and $z/H = 0.07$ and three different axial positions, $x/H = 0.56$, 2.19 and 7.20 , which are located in the upstream, centre, and downstream regions of the central toroidal recirculation zone, respectively. The most dominant mode is 1380 Hz, and other characteristic frequencies include 660 , 2040 , and 3420 Hz. The corresponding wave amplitudes decrease in the downstream region due to dissipation and dispersion effects. These frequencies represent various acoustic modes in the chamber and are determined by the mean flow properties and chamber geometry.

A simple acoustic modal analysis (Morse & Ingard 1986), without accounting for the mean flow effects, indicates that the eigen-frequencies of the first tangential (1T) modes in the dump chamber and the inlet duct are $f_c = 1350$ Hz and $f_i = 2000$ Hz, respectively. They are almost identical to the observed harmonics shown in figure 14. The analysis assumes the speed of sound to be 340 m s^{-1} for air at ambient conditions, and the radii of the inlet duct and the chamber are taken to be 50.8 and 76.2 mm, respectively. The two transverse acoustic modes interact with each other through non-linear gasdynamics to generate a subharmonic and a superharmonic with frequencies

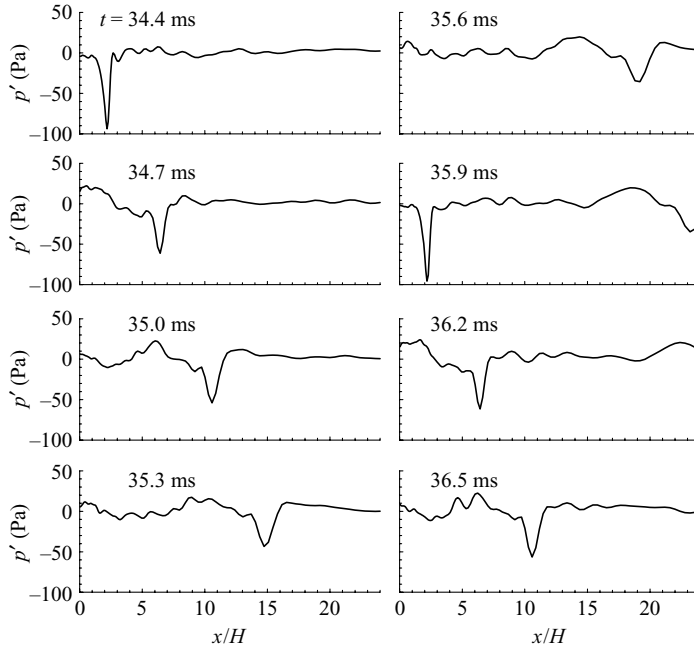


FIGURE 13. Time evolution of fluctuating pressure field spatially averaged over an (r, θ) -cross-section. Swirl number $S = 0.5$.

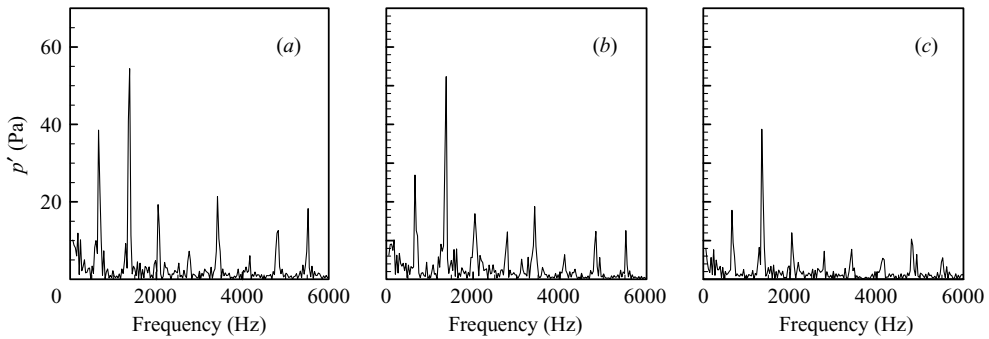


FIGURE 14. Frequency spectra of pressure fluctuations at different axial locations near the centreline: (a) $x/H = 0.38$, (b) $x/H = 2.19$ and (c) $x/H = 7.20$, and $y/H = 0.06$, $z/H = 0.07$. Swirl number $S = 0.5$.

of $f_{s1} = f_i - f_c = 650$ Hz and $f_{s2} = f_i + f_c = 3350$ Hz, respectively. The former propagates in the form of a traveling longitudinal wave as shown in figures 11–13.

The acoustic modal analysis was corroborated using a finite-element software package, ANSYS (ANSYS 2003). The code solves the Helmholtz equation for linear acoustic waves in the entire computational domain without the influence of the mean flow. The results indicate a dominant transverse acoustic mode with an eigenfrequency of 1300 Hz. The corresponding mode shape is shown in figure 15. The first tangential mode prevails in the dump chamber and it induces a degenerated tangential wave in the inlet duct.

To identify the mechanisms of acoustic-wave generation and its relationship with the shear-layer evolution, the vortical flow dynamics need to be further explored. It

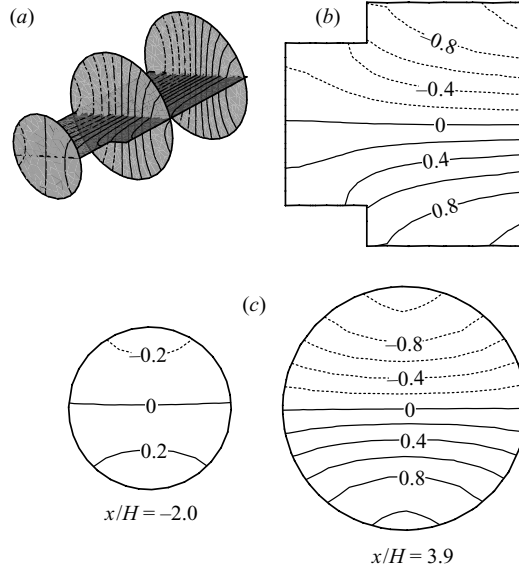


FIGURE 15. First tangential mode of normalized acoustic pressure field in the main chamber with $f_0 = 1300$ Hz, calculated by ANSYS. Solid lines: positive values; dashed lines: negative values. Contour level increases evenly. (a) 3D view, (b) (x, r) -plane, and (c) (r, θ) -cross-sections.

is well established that the shear layer originating from the centrebody is sensitive to external forcing (Wu *et al.* 1998), such as acoustic motion in the chamber. Thus, we may employ shear-layer instability theories to help explain the mutual coupling between the vortical and acoustic motions. Following common practice (Ho & Huerre 1984), the Strouhal number, St , is defined as

$$St = \frac{f_s \delta}{\bar{U}}, \quad \text{with} \quad \bar{U} = \frac{1}{2}(U_1 + U_2) \quad (24)$$

where δ is the initial momentum thickness of the shear layer, and U_1 and U_2 the free-stream velocities on the two sides of the shear layer. The mean averaged axial velocity \bar{U} is approximately 10 m s^{-1} near the trailing edge of the centrebody in the present study. The most unstable mode of an unforced planar shear layer occurs at $St \approx 0.044\text{--}0.048$ for turbulent flows (Ho & Huerre 1984). The momentum thickness δ is roughly one fourth of the vorticity thickness, which can be calculated from the axial velocity profile in the radial direction (Panda & McLaughlin 1994). Based on (24), the frequency of the most unstable mode of shear-layer instability, f_s^0 , is approximately of the order of 10^3 Hz near the downstream region of the centrebody.

For the case with a swirl number of 0.5, the most prevalent acoustic mode shown in figure 14 has a frequency of 1380 Hz, which is consistent with the frequency of the most unstable shear-instability mode. Consequently, the shear layer originating from the centrebody can be easily locked to the first-tangential mode of the acoustic oscillation in the chamber. At this response frequency, f_s^R , the shear layer rolls up into discrete vortices and reinforces the acoustic oscillation in the chamber. A feedback loop between the acoustic fluctuation and shear-layer instability is thus established and leads to a large excursion of flow motions. When the discrete vortices are convected downstream, they pair with the adjacent ones to form larger structures with a characteristic frequency of $f_s^R/2 = 690$ Hz. This subharmonic frequency is also

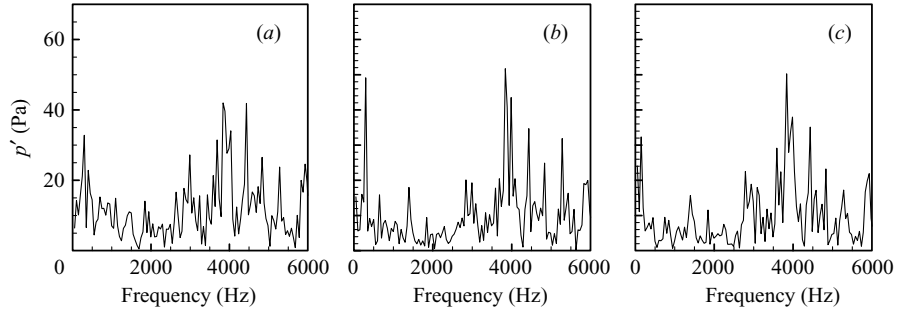


FIGURE 16. Frequency spectra of pressure fluctuations at different axial locations near the centreline: (a) $x/H = 0.38$, (b) $x/H = 2.19$ and (c) $x/H = 7.20$, at $y/H = 0.06$ and $z/H = 0.07$. Swirl number $S = 0.3$.

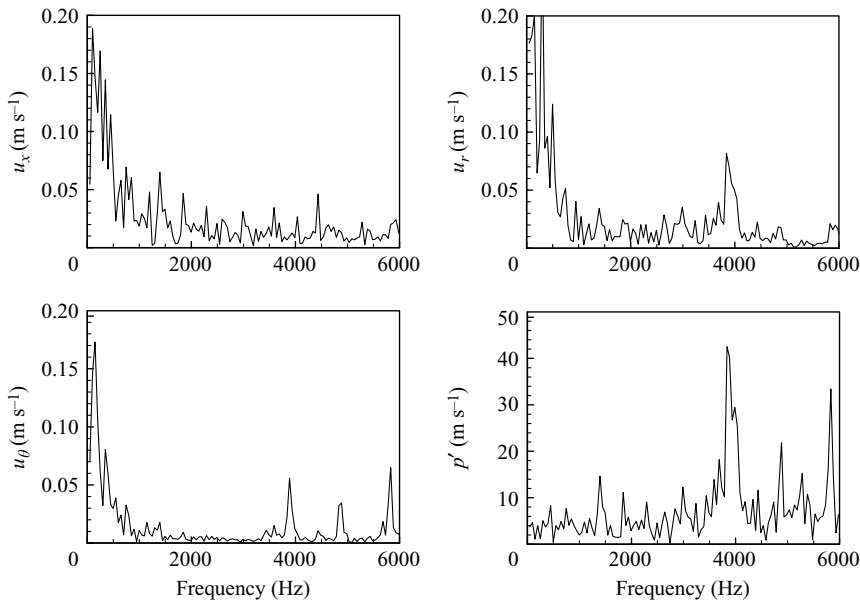


FIGURE 17. Frequency spectra of velocity and pressure fluctuations at $x/H = 0.36$, $y/H = 1.97$ and $z/H = 0.07$. Swirl number $S = 0.3$.

close to the frequency of the longitudinal acoustic mode in the chamber, 655 Hz, as determined from the reduced one-dimensional pressure profiles shown in figure 13.

4.4.2. Effects of swirl number

The effects of swirl number on the acoustic field were examined. Figure 16 shows the frequency spectra of the pressure fluctuations at three different locations for a low swirl number of $S = 0.3$. Compared with the case of $S = 0.5$ (figure 14), the dominant frequency over the entire field is around 3900 Hz, and the well-defined harmonics in the low-frequency range disappear. The corresponding acoustic field is the mixed first tangential (1T) and first radial (1R) mode in the chamber.

An extensive spectral analysis of the velocity and pressure fluctuations in the chamber was conducted to identify the driving mechanism of flow oscillations associated with the vortico-acoustic interaction. Figure 17 shows the result in the region immediately downstream of the trailing edge of the backward-facing step ($x/H = 0.36$,

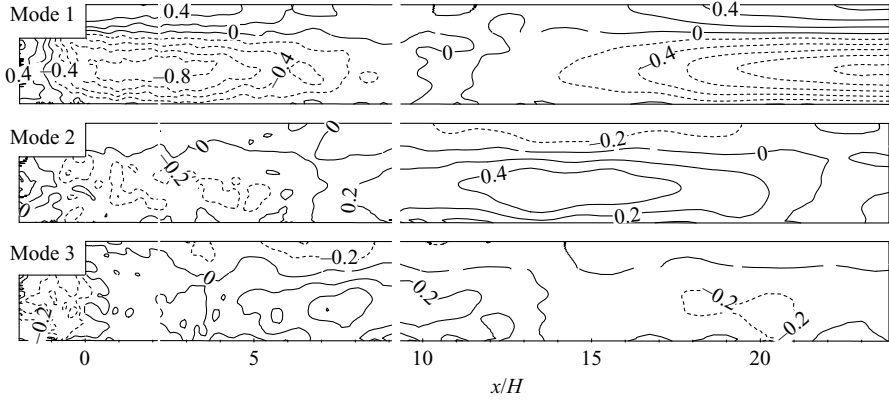


FIGURE 18. First three POD modes of normalized fluctuating pressure field on an (x, r) -plane, Solid lines: positive values; dashed lines: negative values. Contour level increases evenly. Swirl number $S=0.3$.

$y/H = 1.97$, and $z/H = 0.07$). The radial and azimuthal velocity fluctuations are closely coupled with the local pressure oscillation, and exhibit a dominant harmonic at 3900 Hz. The acoustic field interacts effectively with the shear-layer instability at this key position in the flow field, as will be elaborated later. As previously mentioned, the two shear layers originating from the trailing edges of the centrebody and the backward-facing step may exert significant influence on the oscillatory flow characteristics. Their specific effects depend on the swirl number and chamber geometry. At the high swirl number of $S=0.5$, the large vortical structure associated with the central recirculating flow overshadows the shear layer originating from the corner region, and dominates the flow development in the chamber. The resultant acoustic wave thus has a characteristic frequency of 1380 Hz, which matches the frequency of the centrebody shear-layer instability. At a low swirl number of $S=0.3$, no vortex breakdown occurs, and the importance of the flow field on the downstream side of the centrebody in exciting acoustic oscillations diminishes. In contrast, the shear layer in the corner region plays a crucial role in dictating the acoustic flow evolution, whose characteristic frequency of 3900 Hz matches that of the mixed 1T/1R acoustic mode in the chamber.

The acoustic field can be quantitatively analysed using the proper orthogonal decomposition (POD) method to extract energetic coherent structures from the simulation data. For a given pressure field, $p(\mathbf{x}, t)$, the POD analysis can determine a set of orthogonal functions $\varphi_j(\mathbf{x})$, $j = 1, 2, \dots$, so that the projection of p onto the first n functions

$$\hat{p}(\mathbf{x}, t) = \bar{p}(\mathbf{x}) + \sum_{j=1}^n a_j(t)\varphi_j(\mathbf{x}) \quad (25)$$

has the smallest error, defined as $E(\|p - \hat{p}\|^2)$. Here, $a_j(t)$ represents the temporal variation of the j th mode. A more complete discussion of this subject can be found in Berkooz, Holmes & Lumley (1993).

Because of the limitations of data storage, the POD analysis was only conducted for the fields on an (x, r) -plane ($\theta = 0^\circ$) and an (r, θ) -cross-section at $x/H = 1.15$. A total of 220 snapshots spanning a time period of 13 ms were used. Figure 18 shows the three most energetic POD modes on the (x, r) -plane. The first mode reveals a

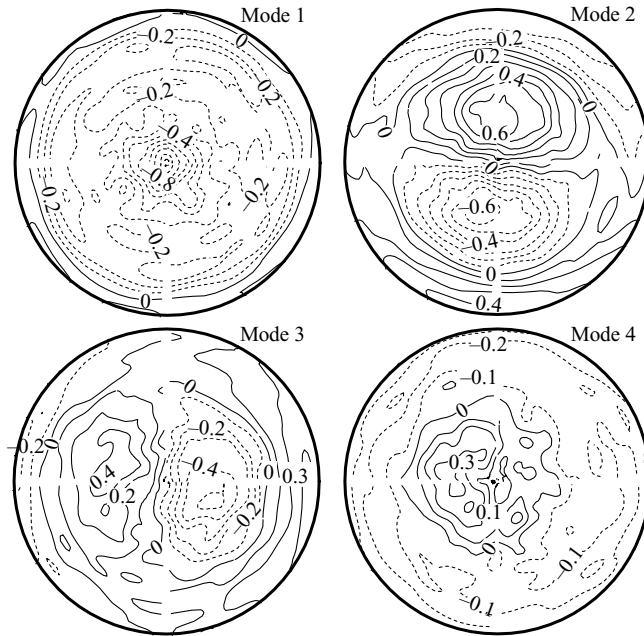


FIGURE 19. First four POD modes of normalized fluctuating pressure field on an (r, θ) -cross-section at $x/H = 1.15$. Solid lines: positive values; dashed lines: negative values. Contour level increases evenly. Swirl number $S = 0.3$.

structure corresponding to the mixed second longitudinal (2L) and first radial (1R) mode of the acoustic wave in the dump chamber, and the first longitudinal (1L) mode in the inlet duct. The dominant frequency of the temporal variation of this POD mode, determined from a separate spectral analysis, is 3900 Hz. The energy carried by this mode contains more than 20% of the total energy of the acoustic pressure field. The POD mode shape indicates the existence of an acoustic pressure node (i.e. $p' = 0$) near the trailing edge of the backward-facing step, where the acoustic velocity reaches its maximum. The same location also experiences a strong shear-layer oscillation, arising from the Kelvin–Helmholtz instability. Thus, the vortex shedding from the edge of the backward-facing step provides a stimulus to drive acoustic motion, especially in the radial direction. This observation is also corroborated by the frequency spectra of acoustic motion given in figure 17.

To obtain a complete picture of the acoustic wave structure, the POD analysis was further applied to examine the situation on a transverse plane. Figure 19 shows the fluctuating pressure field at $x/H = 1.15$. The first mode reveals an axisymmetric structure, which may result from the longitudinal flow motions and noises. Its frequency content shows a broadband distribution. The second and third modes indicate the mixed first tangential (1T) and first radial (1R) mode of the acoustic wave, consistent with the previously observed 1R mode on the (x, r) -plane. These two modes carry about 22% of the total energy of the acoustic pressure field, and are spatially shifted from each other by 90° . Furthermore, they are counter-rotating with respect to the main swirling flow. This result confirms the earlier conclusion with respect to figure 10 that the counter-rotating helical mode is more unstable than the co-rotating mode for a swirl jet (Lessen, Singh & Paillet 1974; Martin & Meiburg 1996). The fourth POD mode corresponds to a radial mode oscillation.

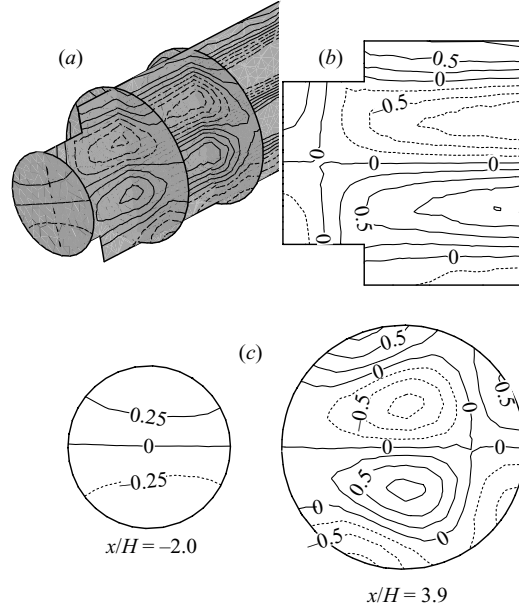


FIGURE 20. Normalized pressure field of acoustic mode with $f_0 = 3982$ Hz, calculated by ANSYS. Solid lines: positive values; dash lines: negative values. Contour level increases evenly. (a) 3D view, (b) (x, r) -plane, and (c) (r, θ) -cross-sections.

Results from the POD analysis of the acoustic fields on both the (x, r) - and the transverse planes lead to the conclusion that the mixed 1L/1T mode prevails in the inlet duct and the mixed 2L/1T/1R mode prevails in the dump chamber. The former has a characteristic frequency of 3879 Hz, and the latter of 3827 Hz. Both frequencies are very close to the dominant frequency of the flow field, $f = 3900$ Hz, as revealed in figures 16 and 17. It should be noted that the acoustic motions in the axial direction, although suggesting a 2L-mode structure as shown in figure 18, are essentially travelling oscillations, because of the implementation of non-reflecting boundary conditions at the chamber exit. Furthermore, owing to the large aspect ratio of the chamber, the frequency of the mixed 1T/1R mode in the chamber, which has a value of 3785 Hz, is only slightly less than that of the 2L/1T/1R mode. The acoustic wave in the chamber is basically dominated by the mixed 1T/1R transverse mode for the case with a low swirl number of $S = 0.3$. The acoustic field obtained from the POD analysis was further compared with the acoustic modal analysis conducted with the ANSYS as shown in figure 20. The mode shapes that are similar to the first POD mode on the (x, r) -plane, and the second and third POD modes on the transverse plane, are observed in the inlet duct and the dump chamber with an eigen-frequency of 3982 Hz. Figure 20 reconstructs the global mode shape in three dimensions and clearly shows that the acoustic mode in each part of the domain is identical to our previous observation in POD analysis. The favourable comparison between the ANSYS prediction and the LES results further corroborated the adequacy of the approach adopted herein.

In general, the boundary conditions at the chamber outlet may significantly modify the longitudinal acoustic motion inside the chamber. The effects of the outlet boundary on the acoustic fields, however, are minor in the present study because the dominant acoustic motions at both swirl numbers are transverse (such as tangential and radial)

oscillations. The acoustic waves originating in the shear layers propagate to the downstream region and eventually exit from the chamber because of the implementation of the non-reflecting boundary conditions at the exit.

5. Summary

Turbulent swirling flows injected into a dump chamber were numerically studied by means of a large-eddy simulation technique. The work simulated the experiment conducted by Favaloro *et al.* (1989). Good agreement was obtained between the measurements and calculated results in terms of mean flow velocities and turbulence properties. Various fundamental mechanisms dictating the flow evolution, including vortex breakdown, Kelvin–Helmholtz instability, and helical instability, were examined systematically for different swirl numbers. In particular, the mutual coupling between the acoustic wave and vortical flow was explored in depth. The unsteady flow evolution was further analysed using a proper-orthogonal-decomposition method and shear-layer instability theories. The swirl number plays an important role in determining vortical flow motions and ensuing acoustic oscillations. Vortex breakdown usually occurs in strong swirling flows, and leads to the formation of a central toroidal recirculation zone in the downstream region of the centrebody. The accompanying shear layer can be easily coupled with the chamber acoustic field, providing a strong stimulus for exciting tangential acoustic motions in both the main chamber and the inlet duct. These two acoustic fields then interact with each other through nonlinear gasdynamics to generate a subharmonic mode travelling longitudinally. The situation, however, becomes drastically different at a low swirl number. Instead of the central recirculating flow, the shear layer originating from the trailing edge of the backward-facing step dominates the acoustic excitation in the chamber. The associated radial velocity fluctuation in the shear layer tends to drive a mixed first tangential and first radial mode of an acoustic wave in the chamber at a much higher frequency. The result has been further corroborated by means of an acoustic analysis using ANSYS.

This work was sponsored by the NASA Glenn Research Center under Grant NAG 3-2151. The support and encouragement of Mr Kevin Breisacher is highly appreciated. The authors also would like to thank Dr Danning You for her help with the acoustic analysis using the ANSYS software. Xiyun Lu was partly sponsored by the National Natural Science Foundation of China (Nos. 90405007 and 10125210).

REFERENCES

- ANSYS, Inc. Corporate 2003 The ANSYS 7.1 Users Documents. <http://www.ansys.com/services/documentation/index.htm>.
- APTE, S. & YANG, V. 2001 Unsteady flow evolution in a porous chamber with surface mass injection, I: free oscillation. *AIAA J.* **39**, 1577–1586.
- BERKOOZ, G., HOLMES, P. & LUMLEY, J. L. 1993 The proper orthogonal decomposition in the analysis of turbulent flows. *Annu. Rev. Fluid Mech.* **25**, 539–575.
- BILLANT, P., CHOMAZ, J.-M. & HUERRE, P. 1998 Experimental study of vortex breakdown in swirling jets. *J. Fluid Mech.* **376**, 183–219.
- BRODA, J. C., SEO, S., SANTORO, R. J., SHIRHATTIKAR, G. & YANG, V. 1998 An experimental study of combustion dynamics of a premixed swirl injector. *Proc. Combust. Inst.* **27**, 1849–1856.
- DESJARDIN, P. E. & FRANKEL, S. H. 1998 Large eddy simulation of a nonpremixed reacting jet: application and assessment of subgrid-scale combustion models. *Phys. Fluids* **10**, 2298–2314.
- FABIGNON, Y., BEDDINI, R. A. & LEE, Y. 1997 Analytic evaluation of finite difference methods for compressible direct and large eddy simulations. *Aerospace Sci. Tech.* **6**, 413–423.

- FALER, J. & LEIBOVICH, S. 1977a An experimental map of the internal structure of a vortex breakdown. *J. Fluid Mech.* **86**, 313–335.
- FALER, J. & LEIBOVICH, S. 1977b Disrupted states of vortex flow and vortex breakdown. *Phys. Fluids* **20**, 1385–1400.
- FAVALORO, S. C., NEJAD, A. S., AHMED, S. A., VANKA, S. P. & MILLER, T. J. 1989 An experimental and computational investigation of isothermal swirling flow in an axisymmetric dump combustor. *AIAA Paper* 89-0620.
- FUREBY, C. 1996 On subgrid scale modeling in large eddy simulations of compressible fluid flow. *Phys. Fluids* **8**, 1301–1311.
- GERMANO, M., PIOMELLI, U., MOIN, P. & CABOT, W. H. 1991 A dynamic subgrid-scale eddy viscosity model. *Phys. Fluids A* **3**, 1760–1765.
- GRABOWSKI, W. J. & BERGER, S. A. 1976 Solution of the Navier-Stokes equations for vortex breakdown. *J. Fluid Mech.* **75**, 525–544.
- GRINSTEIN, F. F., YOUNG, T. R., GUTMARK, E. J., LI, G. Q., HSIAO, G. & MONGIA, H. C. 2002 Flow dynamics in a swirl combustor. *J. Turbulence* **3**, paper 30.
- HO, C.-M. & HUERRE, P. 1984 Perturbed free shear layers. *Annu. Rev. Fluid Mech.* **16**, 365–424.
- HUANG, Y., SUNG, H. G., HSIEH, S. H. & YANG, V. 2003 Large eddy simulation of combustion dynamics of a lean-premixed swirl-stabilized combustor. *J. Prop. Power* **19**, 782–794.
- HUANG, Y. & YANG, V. 2004 Bifurcation of flame structure in a lean-premixed swirl-stabilized combustor: transition from stable to unstable flame. *Combust. Flame* **136**, 383–389.
- JAMESON, A. 1983 The evolution of computational methods in aerodynamics. *Trans. ASME: J. Appl. Mech.* **50**, 1052–1070.
- KIM, W. W., MENON, S. & MONGIA, H. 1999 Numerical simulations of reacting flows in a gas turbine combustor. *Combust. Sci. Tech.* **143**, 25–62.
- LEIBOVICH, S. 1978 The structure of vortex breakdown. *Annu. Rev. Fluid Mech.* **10**, 221–246.
- LEIBOVICH, S. 1984 Vortex stability and breakdown: survey and extension. *AIAA J.* **22**, 1192–1206.
- LESSEN, M., SINGH, P. J. & PAILLET, F. 1974 The stability of a trailing line vortex. Part 1. Inviscid theory. *J. Fluid Mech.* **360**, 753–763.
- LILLY, D. K. 1992 A proposed modification of the Germano subgrid scale closure method. *Phys. Fluids A* **4**, 633–635.
- LUCCA-NEGRO, O. & O'DOHERTY, T. 2001 Vortex breakdown: a review. *Prog. Energy Combust. Sci.* **27**, 431–481.
- MARTIN, J. E. & MEIBURG, E. 1996 Nonlinear axisymmetric and three-dimensional vorticity dynamics in a swirling jet model. *Phys. Fluids* **8**, 1917–1928.
- MARTIN, M. P., PIOMELLI, U. & CANDLER, G. V. 2000 Subgrid-scale models for compressible LES. *J. Theor. Comp. Fluid Dyn.* **13**, 361–376.
- MOIN, P., SQUIRES, K., CABOT, W. & LEE, S. 1991 A dynamic subgrid-scale model for compressible turbulence and scalar transport. *Phys. Fluids A* **3**, 2746–2757.
- MORSE, P. M. & INGARD, K. U. 1986 *Theoretical Acoustics*. Princeton University Press.
- PANDA, J. & MCLAUGHLIN, D. K. 1994 Experiments on the instabilities of a swirling jet. *Phys. Fluids* **6**, 263–276.
- PASCHEREIT, C. O., GUTMARK, E. & WEISENSTEIN, W. 1999 Coherent structures in swirling flows and their role in acoustic combustion control. *Phys. Fluids* **9**, 2667–2678.
- PECKHAM, D. H. & ATKINSON, S. A. 1957 Preliminary results of low speed wind tunnel tests on a Gothic wing of aspect ratio 1.0. *Aero. Res. Council. CP* 508.
- PIERCE, C. D. & MOIN, P. 1998 Large eddy simulation of a confined coaxial jet with swirl and heat release. *AIAA Paper* 98-2892.
- PIOMELLI, U. 1999 Large-eddy simulation: achievements and challenge. *Prog. Aerospace Sci.* **35**, 335–362.
- POINSOT, T. J. & LELE, S. K. 1992 Boundary conditions for direct simulations of compressible viscous flows. *J. Comput. Phys.* **101**, 104–129.
- POLIFKE, W. & WALL, C. 2002 Non-reflecting boundary conditions for acoustic transfer matrix estimation with LES. *Proc. 2002 Summer Program*, CTR, Stanford University.
- RAI, M. M. & CHAKRAVARTHY, S. 1993 Conservative high-order accurate finite difference method for curvilinear grids. *AIAA Paper* 93-3380.
- SALVETTI, M. V. & BANERJEE, S. 1995 *A priori* test of a new dynamic subgrid-scale model for finite-difference large-eddy simulations. *Phys. Fluids* **7**, 2831–2847.

- SARPKAYA, T. 1971*a* On stationary and traveling vortex breakdown. *J. Fluid Mech.* **45**, 545–559.
- SARPKAYA, T. 1971*b* Vortex breakdown in swirling conical flows. *AIAA J.* **9**, 1792–1799.
- SARPKAYA, T. 1995 Turbulent vortex breakdown. *Phys. Fluids* **7**, 2301–2303.
- SARPKAYA, T. & NOVAK, F. 1998 Turbulent vortex breakdown experiments. *IUTAM Symp. Dyn. Slender Vortices* (ed. E. Krause & K. Gersten), pp. 287–296. Kluwer.
- SHTERN, V. & HUSSAIN, F. 1999 Collapse, symmetry breaking, and hysteresis in swirling flows. *Annu. Rev. Fluid Mech.* **31**, 537–566.
- SMAGORINSKY, J. 1963 General circulation experiments with the primitive equations: I. The basic experiment. *Mon. Weather Rev.* **91**, 99–164.
- SPALL, R. E. 1996 Transition from spiral- to bubble-type vortex breakdown. *Phys. Fluids* **8**, 2301–2303.
- SPALL, R. E. & GATSKI, T. B. 1991 Computational study of the topology of vortex breakdown. *Proc. R. Soc. Lond. A* **435**, 321–337.
- WANG, S. 2002 Vortical flow dynamics and acoustic response of gas-turbine swirl-stabilized injectors. PhD Thesis, Pennsylvania State University, University Park, PA, USA.
- WU, J. Z., LU, X. Y., DENNY, A. G., FAN, M. & WU, J. M. 1998 Post-stall flow control on an airfoil by local unsteady forcing. *J. Fluid Mech.* **371**, 21–58.
- YOSHIZAWA, A. 1986 Statistical theory for compressible turbulent shear flows, with the applications to subgrid modeling. *Phys. Fluids* **29**, 2152–2164.
- ZANG, T. A., DAHLBURG, R. B. & DAHLBURG, J. P. 1992 Direct and large-eddy simulations of three-dimensional compressible Navier–Stokes turbulence. *Phys. Fluids A* **2**, 127–140.